CrossMark

Localization and transfer of charge carriers in CuO nanopowder by impedance spectroscopy

A. A. Lepeshev[1,2] · N. A. Drokin[3] · A. V. Ushakov[1,2] · I. V. Karpov[1,2] · L. Yu. Fedorov[1,2] · E. P. Bachurina[1,2]

Abstract

Particular electro-physical characteristics of CuO nanopowder were investigated by impedance spectroscopy using a sensor based on interdigitated structure in the frequency range from 1 Hz to 100 MHz. The results of investigation were considered. Simulation of impedance spectra by equivalent electric circuits was carried out for numerical approximations of the frequency dependences of the dielectrical permittivity and conductivity. Electric charge accumulation of on the boundaries of nanoparticles and near the metal electrodes of the sensor was revealed. It was shown that a double electric layer is formed near the electrodes, which leads to the appearance of anomalously large values of dielectrical permittivity and an increase in the conductivity in the low-frequency region. The obtained results can be explained by proton conductivity in the nanopowder caused by moisture which is adsorbed on the surface of the nanoparticles. It was shown that after high-temperature annealing of CuO nanopowders, accumulation of electric charges was not observed. It was established that hopping or polaron conductivity occurs in the annealed CuO samples, which increases with increasing electric field frequency according to the power law with a fractional exponent.

1 Introduction

Ultra-dispersed media and powders belong to a special class of materials with the advanced and unique properties [1–3]. Production, investigation and explanation of the electro-physical properties of these materials are one of the key tasks in the field of present materials science. Particular attention is paid to the study of copper oxide nanopowder—CuO. This study began with the discovery of high-temperature superconductivity, since copper oxide is the main component of cuprate high-temperature superconductors. At the same time, copper oxide exhibits both magnetic and semiconducting properties. These properties strongly depend both on the production conditions and structure, along with surface of nanoparticles. The parameters of the exchange interaction on the surface change first, thus revealing specific behavior of

the magnetic susceptibility, the temperature dependence of the magnetization, and also the electrical conductivity and the dielectrical permittivity [4–10].

Despite the wide range of works on the study of the magnetic and electrical properties of the CuO nanopowder in the literature, there are still no ideas about the processes of electric polarization, motion and localization of charge carriers in the volume of matter and on the surface of nanoparticles. This gap can be explained by the fact that each sample of CuO nanopowder has its unique properties, which depend not only on the bulk structure of the material, but also on the difficultly predictable state of the surface on which there are structural lattice defects as well as adsorbed gases and moisture. In addition, in the initial powder, a spontaneous agglomeration of nanoparticles occurs, which is accompanied by a change in the structure of the agglomerate surface and the appearance of internal mechanical stresses.

To date, the magnetic and electrical characteristics of copper oxide have been experimentally studied using specially prepared samples produced by hot pressing [11], sintering of the initial nanopowder at high temperatures [12]. Single crystals of CuO [13, 14] and thin films on the dielectric substrate [15, 16] have also been investigated, and even structures in the form of nanorods and nanowires have been created [17, 18]. However, the electro-physical properties of

✉ A. A. Lepeshev
sfu-unesco@mail.ru

1 Krasnoyarsk Scientific Center of the Siberian Branch of the Russian Academy of Science, Krasnoyarsk, Russia 660036

2 Siberian Federal University, Krasnoyarsk, Russia 660041

3 Siberian Branch, Kirensky Institute of Physics, Russian Academy of Sciences, Krasnoyarsk, Russia 660036

all these CuO samples are highly unique and mainly depend on the technological conditions and the methods of the material production. Direct measurement of physical characteristics of nanoparticles is a complex challenge; however, the initial certification of nanopowders proves to be necessary, since it can function as a link in the production chain of materials based on copper oxide and their applications.

This study is aimed at the investigation of electrical and dielectric properties of copper monoxide nanopowder by impedance spectroscopy using a special sensor made on the basis of interdigitated structure. The main task of the work is to determine and analyze the impedance and electro-physical characteristics of CuO nanopowder in the initial state as well as after its compaction and annealing at a temperature of 300 °C.

2 Materials and physical measurements

In this study, a plasma-chemical method was used for production of powder CuO compounds. This method is based on evaporation of a cathode from massive copper in a low-pressure arc discharge plasma with further condensation of plasma-chemical reaction products on a substrate.

The synthesis of CuO nanopowder was performed in a plasma-chemical reactor, described in [19, 20]. The arc evaporator, used in the process, had the following characteristics: a current arc of 100 A, an intensity of the longitudinal magnetic field excited by a focusing coil on the surface of the cathode, of 80 A/m, with a distance between the cathode and the anode of $d = 50$ mm. A rod, made of high-purity copper (99.99%) with a diameter of 80 mm and a length of 100 mm, was used as a sputtering cathode. It was placed on a water cooled copper current lead. In order to begin plasma chemical reactions, the chamber gas was preliminary pumped out to a pressure of $p = 1$ mPa and then it was filled

by a gas mixture containing 40 vol% O_2 from N_2 plasma-generating gas in the input. To study the pressure influence, nanoparticles were synthesized at a basic pressure of 80 Pa. Oxygen was supplied to the reactor in order to form a uniform layer around the plasma torch. The reaction products were collected during 10 min on a hemispherical collector made of water-cooled stainless steel, placed at a distance of 0.12 m from the cathode. Table 1 describes the operating parameters of the reactor during the synthesis.

The morphological composition of the samples was studied by transmission electron microscope JEOL JEM-2100. Studying the phase composition of the samples was carried out using Advance D8 X-ray diffractometer in CuKα monochromatic radiation. Scanning was performed at room temperature in the range of angles at 30–70 deg with 2θ step of 0.06 deg.

To measure complex resistance (impedance) of powder materials, a special sensor of capacitive type was made and placed on a polycor substrate with a thickness of $h = 1$ mm and a size of 17×22 mm (Fig. 1). The bottom metallized side of the substrate (1) was soldered to a metal substrate which acted as a shield. On the upper side of the substrate an interdigital structure consisting of four pairs of pins with a length of $l = 7$ mm, a width of $h = 0.5$ mm and a distance between the pins of $d = 0.2$ mm (2) was formed by chemical etching. A glass border of 10 mm high (3) was placed around the interdigital structure into which nanopowder was added, and then it was sealed with a glass piston. The height of the compacted powder must be at least 3 mm from the surface of the electrodes. This type of sensor can operate in a wide frequency range of ~ 0.1 Hz–100 MHz and it is convenient to be used to test not only bulk substances but also liquid ones [21, 22].

For the measurements, the sensor was connected through the contacts (4) to the Elins 1500 and Agilent E5061B impedance analyzers operating in the frequency range from 0.1 Hz

Table 1 Operating parameters of the vacuum plasma-chemical reactor for CuO synthesis

Parameter	Conditions
Residual pressure in chamber	10^{-3} Pa
Arc discharge current	100 A
Voltage	70 V
Power	10 kW
Operating pressure of gas mixture	80 Pa
Supply of reaction gas (oxygen)	40 vol% O_2
Maximum permissible temperature of the device for condensation of powder, K	300
Maximum permissible amount of impurities of the cathode material, %	< 0.01
Rated current of high-voltage power supply of arc evaporator, kA	2.3
Current of stationary discharge, A	20–500
Frequency of pulsed arc discharge, Hz	100
Pulse duration, μs	250
Passivation time of produced nanopowder, days	1

Fig. 1 Measuring cell with an interdigital structure. 1—quartz substarate, 2—interdigital structure, 3—glass border, 4—conductor path
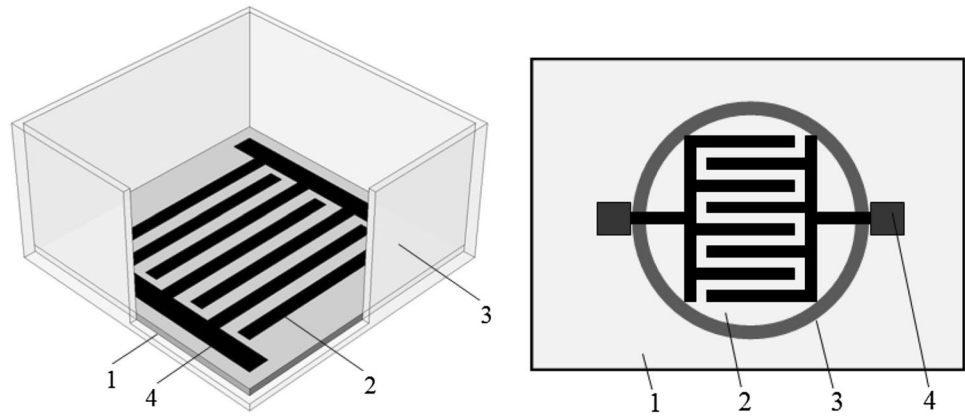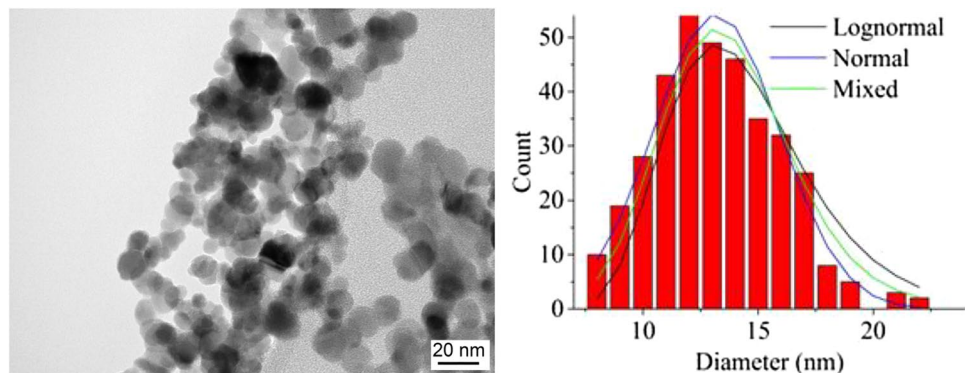

to 1 MHz and from 5 Hz to 100 MHz respectively. The amplitude of the sinusoidal voltage was chosen in the range of 200–250 mV. The measurement technique involves recording the frequency dependences of the impedance modulus $|Z(f)|$ and the angle of the phase shift $\phi(f)$ between the current and the voltage. These data allows to calculate the real $Z'(f) = |Z(f)| \cdot \cos\phi(f)$ and the imaginary $Z''(f) = |Z(f)| \sin\phi(f)$ components of the impedance which are then used to calculate the frequency dependencies of the effective resistance $R_{eff}(f)$, the capacity $C_{eff}(f)$ and other electro-physical characteristics of the material under study. To determine the frequency dependence of the complex dielectric permittivity (DP) of the materials $\varepsilon^*(f)$, a preliminary calibration of the sensor was performed based on recording the change in the electric capacity of the empty sensor $C_0 = 6.2$ pF while the cuvette was filled with the test liquids: chloroform ($\varepsilon = 4.8$), dichloroethane ($\varepsilon = 10.36$) and isopropyl alcohol ($\varepsilon = 18$) in the entire frequency range. The Eqs. (1, 2) were used to calculate the frequency dependences of the effective resistance and the capacity of the sensor.

$$R_{eff}(f) = Z'(f)\left[1 + \left(\frac{Z''(f)}{Z'(f)}\right)^2\right], \qquad (1)$$

$$C_{eff}(f) = \frac{Z''(f)}{\omega R_{eff}(f) Z'(f)}. \qquad (2)$$

where $\omega = 2\pi f$ is the angular frequency [23–25]. This calibration allows calculating the frequency dependence of the complex dielectric permittivity $\varepsilon^*(f)$ of the mixture powder with the air within accuracy $\pm\,0.1$. In this work, the initial CuO powders were used, which were then annealed in air for 10 h at the temperature of 300 °C.

3 Results and analysis

Figure 2 shows the TEM images, histogram, and probability density functions of nanosized copper oxide nanoparticles produced at the pressure of the gas mixture (40 vol% $O_2 + 60\%$ N_2) of 80 Pa.

It is obvious from the results above, that the produced powder represents strongly agglomerated particles of a spherical shape. The particle size ranges from 5 to 20 nm. The combination of normal and log-normal size distributions characterizes these particles. This suggests two competing mechanisms of particle condensation from a steam-plasma phase: cluster and steam condensations. The mixed density function under study represents the sum of the density functions of lognormal and normal distribution with adjustable parameters. It is obvious from the figure above, that this function describes the particle size distribution much better. The average particle size was 12.4 nm, the mean mass

Fig. 2 TEM images, histogram, and probability density functions of nanosized copper oxide powders produced under the pressure of the gas mixture (40 vol% $O_2 + 60\%$ N_2) equal to 80 Pa

particle size was 13.2 nm, and the standard deviation was 1.18.

Nanopowders are characterized by a high surface energy, which is compensated by a significant aggregation of powders, and this process causes a significant decrease of the specific surface. Since the nanoparticle synthesis in a plasmachemical reactor is always accompanied by definite chemical processes, the size distribution function of nanoparticles becomes more complicated because of the products of these reactions. The morphology of the particles also becomes more complicated and various particles of different chemical composition are formed. Besides, interdiffusion of nanoparticles in the condensed phase occurs. Under a sufficiently high temperature, multiple processes can occur simultaneously, forming strong coupling between the nanoparticles. The experimental data are described by a normal distribution while prevailing nanoparticles layered growth due to the adsorption of atoms and the diffusion processes during corresponding atomic mass transfer at the interface.

Figure 3 shows the X-ray diffraction pattern of nanoparticles, synthesized under the pressure of the gas mixture (40 vol% O_2 + 60% N_2) for the values of 2θ in the range from 30 to 70 deg. The figure also shows the XRD of copper oxide nanopowders annealed during 10 h at 300 °C in air.

The XRD pattern clearly illustrates that the copper oxide nanoparticles, formed during the synthesis, have a crystalline nature, and monoclinic crystal structure of CuO (PDF 4 + #00-045-0937) with lattice parameters of a = 4.691 Å, b = 3.432 Å, and c = 5.138 Å.

After annealing copper oxide nanoparticles at 300 °C for 10 h, the lines of reflexes narrowed and their intensity increased, indicating a possible agglomeration of nanoparticles and their preliminary sintering.

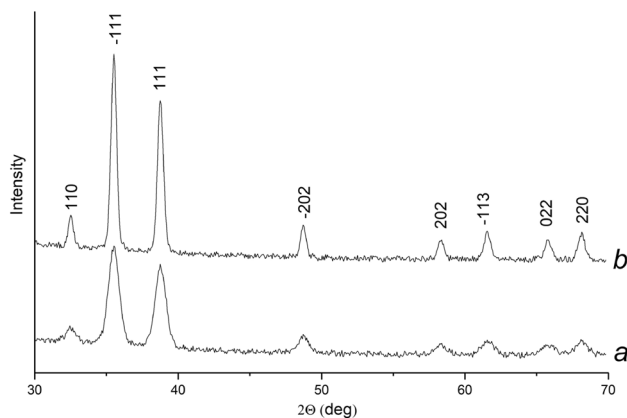Impedance spectroscopy involves presenting the results in the form of a Bode graph. This graph is a combination of the frequency dependence of the impedance modulus |Z(f)| and the displacement angle between the current and the voltage $\phi(f)$. Figure 4 shows a graph resulting from the measurement of the impedance of the sensor with a compressed CuO powder (P = 20 kPa). The measurement was performed at room temperature.

As can be seen from Fig. 4, the total complex resistance of the powder (1) at a frequency of $f = 0.1$ Hz reaches the value of |Z| = $2 \cdot 10^7$ Ohm, but then monotonically decreases with increasing frequency, and at a frequency of $f = 100$ MHz |Z| it is equal to 200 Ohm. This impedance value is actually determined by the high-frequency capacity of the sensor with nanopowder, which at a frequency of 100 MHz has a value of $C_{hf} = 7.2 \cdot 10^{-12}$ F, and the phase angle $\phi = -89°$ approaches to the limiting value of $-90°$. As the frequency decreases, the angle ϕ decreases, but in the frequency range of $f = 350$ Hz and $f = 20$ Hz, some inflection points appear, and at the lowest frequency of $f = 0.1$ Hz the phase angle has a value of $\phi \approx -15°$. Such a phase shift between the current and the voltage at an extremely low frequency can occur only in the case of a strong increase in the electrical capacity of the sample. The reason for this increase in capacity can be explained by the accumulation of electrical charges near the electrodes.

These charges create a double electric layer that shields the external electric field and this is perceived as an apparent increase in the electrical capacity of the sample. It is rather difficult to determine the electro-physical characteristics of this region from the analysis of the measured impedance spectra. However, a more obvious representation of the electro-physical characteristics of the studied material can be obtained by an impedance hodograph, which is the dependence of the imaginary component of the impedance (Z″) on the actual ones (Z′) for the whole set of frequencies. With this representation of the impedance, the correspondence of the shape of the hodograph to the certain electrical
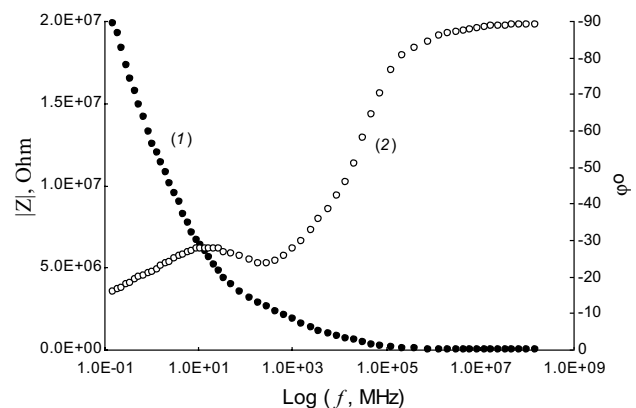

Fig. 3 XRD pattern of copper oxide nanopowder produced under the pressure of the gas mixture (40 vol% O_2 + 60% N_2) equal to 80 Pa (a) and after annealing at 300 °C, t = 10 h

Fig. 4 Frequency dependence of the impedance modulus |Z|(f) (1) and the phase ϕ (f) (2) of the initial compacted CuO nanopowder

circuit was analyzed. The active and reactive elements of the circuit were compared with the probable mechanisms of motion and polarization of electric charges in the material under study. The hodograph of the given nanopowder impedance is shown in Fig. 5. The arrow indicates the direction of increasing frequency, and each point corresponds to the certain frequency.

The hodograph represents an increasing sequence of experimental points, which at the origin of coordinates in the high-frequency region forms a poorly discernible part of the arc of the semicircle, and with decreasing frequency, the points lie on a straight line. Due to the high electrical resistivity of the nanopowder, the accuracy of impedance measurements is reduced, so the low-frequency points of the hodograph are highly scattered. This type of hodograph can be simulated by a simple equivalent electric circuit shown in the inset in Fig. 5. The circuit contains only two elements: capacity C and a special frequency-dependent element designated as *CPE* (*constant phase element*) [21, 26]. The capacity C was introduced into the circuit to approximate the initial (high-frequency) part of the hodograph, and the approximation of the low-frequency ray of the hodograph was carried out with an artificial *CPE* element. The impedance of this artificial *CPE* element is set by the following equation:

$$Z_{CPE} = \frac{1}{A(i\omega)^{\eta}} = \frac{1}{A\omega^{\eta}}\left[\cos\left(\eta\frac{\pi}{2}\right) - i\sin\left(\eta\frac{\pi}{2}\right)\right]. \quad (3)$$

where A is the proportionality coefficient, i is the imaginary unit, and $0 < \eta < 1$ is the exponent that formally characterizes the non-uniform distribution of electric charges over the volume of the material. This element is intended for modeling the distributed properties of substances and has both the real and imaginary components of the impedance. Numerical calculation of the nominal values of this
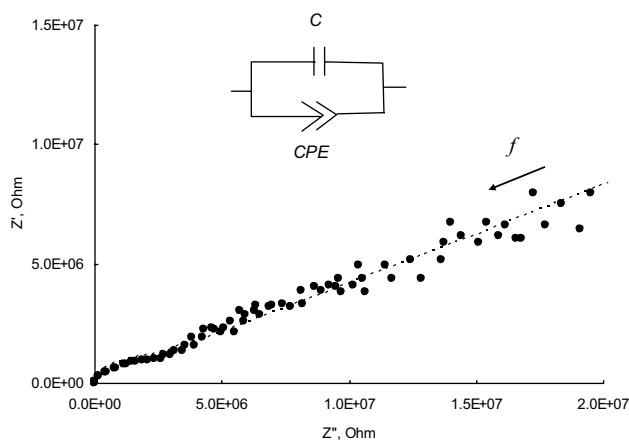
equivalent circuit was carried out using a special software *EIS Spectrum Analyzer*. The calculated value of the capacity of the equivalent circuit $C = 1 \cdot 10^{-11}$ F is in good agreement with the experimentally measured high-frequency capacity of the nanopowder $C_{hf} = 8.8 \cdot 10^{-12}$ F. The coefficient $A = 5 \cdot 10^{-8}$ and the exponent $\eta = 0.25$ was obtained for the *CPE* element. Depending on the exponent, this element can be considered as a conventional capacitor at $\eta = 1$ or as a conventional resistor at $\eta = 0$. For fractional values of $0 < \eta < 1$, this element is treated as a set of frequency-dependent resistor and frequency-dependent capacity. In this case, the dimension of Z_{CPE} can be written as (Ω^{-1} s$^{\eta}$). The exponent $\eta = 0.25$ obtained from the calculation means that the *CPE* element corresponds to the frequency-dependent resistor rather than to the frequency-dependent capacity.

When this element was introduced into the equivalent scheme, the certain fact was taken into account. The fact is that the nanopowder in the measuring cell should be considered as a spatially inhomogeneous (fractal) structure of nanoparticles and their agglomerates with air interlayers. Apparently, the preliminary compaction of the nanopowder in the measuring cell leads to the formation of highly inhomogeneous regions with large air gaps between the separate nanoparticles or agglomerates. As the impedance hodograph shows, even such a structure can strongly polarize in an alternating electric field, since the inclined ray of the hodograph indicates the accumulation of electric charges most likely on the surfaces of neighboring nanoparticles. Due to the high degree of heterogeneity of the compacted nanopowder, the shape of the impedance hodograph looks blurred.

To increase the homogeneity, an additional compression of the nanopowder at a pressure of $P = 120$ kPa was carried out. The impedance hodograph of the compressed nanopowder, obtained from the experiment, is shown in Fig. 6. The same figure shows an equivalent scheme for the numerical approximation of the hodograph.

First, it can be seen that the components of the impedance $Z'(f)$ and $Z''(f)$ (f) have significantly decreased in magnitude, since a closer contact of the nanoparticles during the compression of the powder obviously contributes to a decrease in the contact resistance between them. The experimental points of the hodograph form a well-defined arc of the semicircle at high frequencies and an increasing low-frequency beam. The equivalent electric circuit, shown in the inset in Fig. 6, is well suited for the numerical approximation of this hodograph. It consists of three parallel circuits. One of the circuits contains the capacitor $C_1 = 1 \cdot 10^{-11}$ F, which also simulates a high-frequency capacity. The second circuit contains the resistance $R_1 = 8 \cdot 10^5$ Ohm, simulating static resistance of a compressed nanopowder. The third circuit contains two series-connected elements, a resistance $R_2 = 24$ kOhm, and the *CPE* element with the coefficient $A = 4.94 \cdot 10^{-7}$ F^{-1}
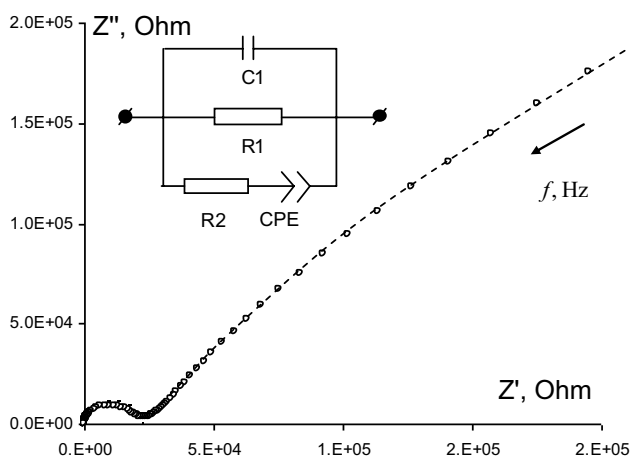

Fig. 5 Hodograph of the impedance of compacted (P = 20 kPa) CuO nanopowder

Fig. 6 The impedance hodograph of the compressed (P = 120 kPa) CuO nanopowder. Dotted line shows numerical approximation of the hodograph
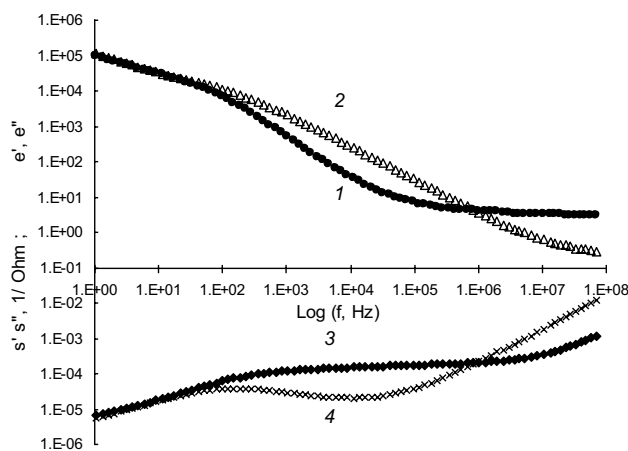

Fig. 7 Frequency dependence of the real (1) and the imaginary (2) components of DP and the conductivity components (3) and (4) of the compressed CuO nanopowder (P = 120 kPa)

s^η and $\eta = 0.63$. This value of the exponent shows that this *CPE* element can now be compared with a distributed capacity which at low frequencies could have formed near the electrodes of the measuring cell due to the increased conductivity and the accumulation of electric charges. Resistance R_2 probably simulates the electrode process of charge exchange with an external electrical circuit. Within the framework of a simple model, the accumulation of charges on the electrode surface can be explained by the presence of a potential barrier that prevents exchange of charges between ions and a metal electrode. Such accumulation of charges near the electrodes and, possibly, on the boundaries of the nanogranules, inevitably shields the external electric field, which is perceived in the experiment as an apparent low-frequency increase in the capacity and complex dielectrical permittivity of the nanopowder $\varepsilon^*(f)$ [22]. Figure 7 shows the frequency dependences of the real and imaginary components of DP calculated from the Eqs. (4–7) as well as the corresponding conduction components of the compressed CuO nanopowder (P = 120 kPa).

$$\varepsilon\prime(f) = \varepsilon^*(f) \cdot Sin(\varphi), \tag{4}$$

$$\varepsilon''(f) = \varepsilon^*(f) \cdot Cos(\phi). \tag{5}$$

$$\sigma'(f) = \varepsilon'' \varepsilon_0 \omega. \tag{6}$$

$$\sigma''(f) = \varepsilon' \varepsilon_0 \omega. \tag{7}$$

In the high-frequency range from 10^5 to 10^8 Hz, the real component of DP (1) is located in the range of $\varepsilon' \sim 4.2$–3.13, and the imaginary component of DP, which characterizes the dielectric losses, is located in the range of $\varepsilon'' = 0.3$. As the frequency decreases, both the real and imaginary components of DP increase to enormous values of $\varepsilon' \approx \varepsilon'' = 1 \cdot 10^5$. Such an increase in DP components in the low-frequency

region is accompanied by significant changes in the behavior of the frequency dependence of the through conductivity, mainly at low frequencies. The decrease in the real component of conductivity (4) is obviously can be referred to the localization of charges near the surface of the electrodes, and the nonlinear behavior of the imaginary component of the conductivity occurs due to the increase in the near-electrode capacity when the frequency decreases.

It can be assumed that the formation of near-electrode and surface charges is facilitated by proton conductivity. This conductivity occurs because of the moisture adsorbed on the surface of the nanoparticles due to the generation and transporting of H_3O^+ and OH^- ions through the relay mechanism of H^+ proton transfer along the chain of water molecules. It can be assumed, that under the condition of presenting this type of conductivity, the adsorbed moisture would evaporate and the accumulation of charges at the electrodes would stop during the nanopowder annealing at high temperatures. To test this assumption, the CuO nanopowder was annealed in air at t = 300 °C for 10 h. The hodograph of the annealed nanopowder impedance is shown in Fig. 8.

As can be seen from Fig. 8, no low-frequency ray of the impedance hodograph appear after nanopowder annealing. The bulk resistive-capacitance characteristics of the nanopowder form an almost regular semicircle that is well simulated by the equivalent electric circuit shown in the inset in Fig. 6. Since the electro-physical properties of the nanopowder after annealing turn to be closely related to the disordered structure of the nanogranules and their agglomerates, a frequency-dependent element *CPE*, reflecting the fractal structure of the material, is used to simulate the electrical polarization process. The process of charge transfer between the electrodes from granule to granule in this electrical circuit was simulated by the conventional resistance *R*. Figure 8
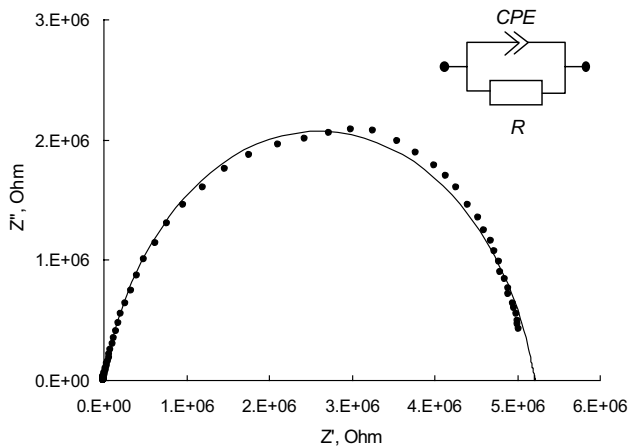
Fig. 8 Impedance hodograph of CuO nanopowder annealed at 300 °C. The solid line represents the hodograph approximation
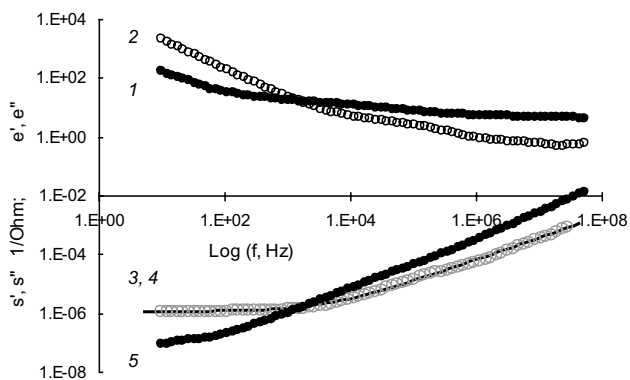

Fig. 9 Frequency dependence of the real and imaginary components of DP (1), (2) and the conductivity (3), (5) of the annealed CuO nanopowder. Line (4) shows the approximation of the real component of the conductivity

(the solid line) shows the result of approximating the impedance hodograph using this equivalent circuit with parameters $A = 4.94 \cdot 10^{-7}$ F^{-1}, exponent $\alpha = 0.67$ and resistance $R = 5.2 \cdot 10^6$ Ohm. Because of the absence of proton conductivity after annealing, the residual resistance of the annealed nanopowder R can be explained by the presence of aliovalent copper ions on the surface of nanoparticles between which either the exchange of electrons or holes is possible or the polaron type of conductivity is realized, which was earlier discussed in [13, 19, 23]. The frequency dependence of the real and imaginary components of DP and the conductivity, calculated from the impedance measurements, are shown in Fig. 9.

While comparing these results with the data shown in Fig. 7, it is becomes obvious that in the low-frequency region the real component of DP does not increase so much compared to the frequency decrease, and at $f = 10$ Hz it gives

a value of $\varepsilon' = 35$, and at a high frequency it gives a value of $\varepsilon' = 4.2$. The imaginary component of DP at a high frequency gives a value of $\varepsilon'' = 0.18$, but decreases monotonically in the logarithmic coordinates to the value of $\varepsilon'' = 420$. This increase in $\varepsilon''(\omega)$ is due to the presence of active conductivity, frequency dependence of which is shown in Fig. 7 (3). As can be seen, the real component of conductivity remains a constant and equal to $\sigma' = 2 \cdot 10^{-7}$ Ohm^{-1} only in the frequency range from 10 Hz to 2 kHz, and then begins to increase in accordance with the Eq. (8) [22, 26].

$$\sigma'(\omega) = \sigma_{dc} + B\omega^s \qquad (8)$$

where σ_{dc} is the static value of the conductivity, B is the proportionality coefficient, and the exponent is $0 < S < 1$. The results of approximating the real component of conductivity $\sigma'(\omega)$ are shown in Fig. 7 by the dotted line obtained with the following values: static specific conductivity $\sigma_{dc} = 2 \cdot 10^{-7}$ 1/·Ωm·m, coefficient $B = 5 \cdot 10^{-10}$ and $S = 0.75$. It is obvious that the theoretical dependence of $\sigma'(\omega)$ according to the Eq. (8), agrees rather well with experiment over the entire frequency range. Such an increase in the real component of the conductivity at high frequencies is typical of materials possessing hopping and possibly polaron conductivity.

4 Conclusion

Based on the analysis of impedance spectra in various graphical representations, the possible mechanisms of polarization, conductivity, and the accumulation of electrical charges near the electrodes has been studied. The numerical values of the capacitive and resistive characteristics of nanoparticles have been determined by simulation of impedance spectra using equivalent electric circuits. The values of the real and imaginary components of the dielectrical permittivity of the nanopowder have been calculated. They reached enormous values of ε', ε'' ~10^6 in the low-frequency region, and decreased to $\varepsilon' \approx 3$, $\varepsilon'' \approx 0.3$ while the frequency increased. It has been shown that a space-charge region appears in the frequency range $f < 100$ Hz near the electrodes of the measuring cell, which leads to an anomalous increase in the real and imaginary components of DP.

It has been established that after the thermal annealing of the nanopowder at the temperature of 300 °C the volumetric charges do not arise near the electrodes. This fact led to the conclusion that moisture in the initial nanopowder, adsorbed on the surface of nanoparticles, contributed to the appearance of proton conductivity and the accumulation of charges near the electrodes. The electrical conductivity of the annealed nanopowder can be explained by the mechanism of hopping or polaron conductivity with the participation of aliovalent copper ions.

References

1. Mohammad Eghbali-Arania, A. Sobhani-Nasabb, Mehdi Rahimi-Nasrabadic, Farhad Ahmadid, Saeid Pourmasoud, Sonochemistry **43**, 120 (2018)
2. A. Saeid Pourmasoud, M. Sobhani-Nasab, Behpour, Mehdi Rahimi-Nasrabadi, Farhad Ahmadi. Jof Mol Struct **1157**, 607 (2018)
3. Seyed Sajjad Hosseinpour-Mashkani, Ali Sobhani-Nasab, J. Mater. Sci. **28**, 16459 (2017)
4. T.I. Arbuzova, S.V. Naumov, V.L. Arbuzov, K.V. Shalnov, A.E. Ermakov, A.A. Mysik, Phys. Solid State **45**, 290 (2003)
5. A.E. Ermakov, M.A. Uymin, A.V. Korolyov, K.N. Mikhalev, A.N. Pirogov, A.E. Teplikh, N.N. Schegoleva, V.S. Gaviko, I.V. Byzov, V.V. Maikov, Phys. Solid State **57**, 283 (2015)
6. J. Koshy, S. Samuel, A. Chandran, P. Vijayan, K.C. George, Inter. J. Chem. Phys. Sci. **4**, 71 (2015)
7. A.V. Ushakov, I.V. Karpov, A.A. Lepeshev, J. Supercond. Novel Magn. **30**, 3351 (2017)
8. A.A. Lepeshev, A.V. Ushakov, I.V. Karpov, D.A. Balaev, A.A. Krasikov, A.A. Dubrovskiy, D.A. Velikanov, M.I. Petrov, J. Supercond. Novel Magn. **30**, 931 (2017)
9. A.A. Lepeshev, A.V. Ushakov, I.V. Karpov, J. Appl. Phys. **122**, 104103 (2017)
10. A.V. Ushakov, I.V. Karpov, A.A. Lepeshev, M.I. Petrov, J. Appl. Phys. **118**, 023907 (2015)
11. X. Rocquefelte, K. Schwarz, P. Blacha, S. Kumar, J. van den Brink, Nature Communications **4**, 2511 (2013)
12. A. Punnoose, H. Magnone, M.S. Seehra, Phys. Rev. B **64**, 174420 (2001)
13. Y. Bowen, S. Ramesh, C. Gill, S. Lawson, J. Mater. Sci. **33**, 5103 (1998)
14. A.A. Samokhvalov, T.I. Arbuzova, V.V. Osipov, N.A. Viglin, S.V. Naumov, N.I. Solin, B.A. Gizhevsky, I.B. Smolyak, V.A. Teplov, V.P. Pilyugin, Phys. Solid State **38**, 3277 (1996)
15. A. Bose, S. Basu, S. Banerjee, D. Chakravorty, J. Appl. Phys. **98**, 074307 (2005)
16. D.-D. Wang, F.-Z. Zhou, J.-X. Cao, L.-B. Li, G.-L. Li, Curr. Appl. Phys. **17**, 781 (2017)
17. A.A. Samokhvalov, N.A. Viglin, B.A. Gizhevskii, N.N. Loshkareva, V.V. Osipov, N.I. Solin, Yu..P. Sukhorukov, J. Exp. Theor. Phys. **103**, 951 (1993)
18. V.V. Osipov, I.V. Kochev, S.V. Naumov, J. Exp. Theor. Phys. **5**, 1246 (2001)
19. A.V. Ushakov, I.V. Karpov, A.A. Lepeshev, L. Yu. Fedorov, A.A. Shaikhadinov, Int. J. Nanosci. **15**, 1550027 (2016)
20. A.V. Ushakov, I.V. Karpov, A.A. Lepeshev, M.I. Petrov, Vacuum. **133**, 25 (2016)
21. B. Purusottam Reddy, K. Sivajee Ganavesh, O.M. Hussain, Appl. Phys. A **122**, 128 (2016)
22. A. Moumen, B. Hartiti, P. Thevenin, Opt. Quant. Electron. **49**, 70 (2017)
23. T. Jiang, M. Bujoli-Doeuff, Y. Farre, Y. Pellegrin, E. Gautron, M. Boujtita, L. Cario, S. Jobic, F. Odobel, RSC Adv. **6**, 1549 (2016)
24. J.R. Macdonald, J. Non-Cryst. Solid **197**, 83 (1996)
25. F.L. Dickert, G.K. Zwissler, B. Bunsenges, Phys. Chem. **97**, 184 (1993)
26. J. Koshy, S.M. Soosen, A. Chandran, K.C. George, J. Semicond. **36**, 122003 (2015)